Nano Research

Open Access

Research Article

CoFe alloy embedded in ultra-thin nitrogen-doped carbon nanosheets derived from CoFe LDH as efficient oxygen reduction electrocatalyst for Zn-air batteries

Peilin Liu[2,§], Yuanqing Sun[1,2,§ ✉], Jiaqing Luo[2], Zehua Dong[2], Peng Zhang[6], Shaoming Zhong[2], Yuechang Wei[1,2], Weiyu Song[1,2], Yu Wang[5 ✉], Zhenxing Li[1 ✉], Zhen Zhao[1,4], and Jian Liu[1,3 ✉]

[1] *State Key Laboratory of Heavy Oil Processing, China University of Petroleum, Beijing 102249, China*
[2] *College of Science, Beijing Key Lab of Oil and Gas Optical Detection Technology, and Basic Research Center for Energy Interdisciplinary, China University of Petroleum, Beijing 102249, China*
[3] *State Key Laboratory of Heavy Oil Processing at Karamay, China University of Petroleum Beijing at Karamay, Karamay 834000, China*
[4] *Institute of Catalysis for Energy and Environment, College of Chemistry and Chemical Engineering, Shenyang Normal University, Shenyang 110034, China*
[5] *Department of Chemistry, School of Science, Westlake University, Hangzhou 310024, China*
[6] *Petrochemical Research Institute, PetroChina Company Limited, Beijing 102206, China*
[§] *Peilin Liu and Yuanqing Sun contributed equally to this work.*

Cite this article: *Nano Research*, **2025**, *18*, 94907139. https://doi.org/10.26599/NR.2025.94907139

ABSTRACT: In response to alleviate the escalating environmental pollution and energy scarcity, the development of a cost-effective, efficient and stable bifunctional oxygen reduction reaction/oxygen evolution reaction (ORR/OER) electrochemical catalyst for new energy conversion devices holds significant value. In this context, we present a two-step hydrothermal/annealing synthesis approach of CoFe alloy nanoparticles on nitrogen-doped ultra-thin carbon nanosheets as an excellent ORR/OER bifunctional catalyst. The hydrothermal process facilitates the intercalation of CoFe layered double hydroxide (CoFe LDH) onto the nitrogen-doped ultra-thin carbon layer, followed by an *in-situ* transformation into carbon-coated nano-alloy particles (Co_3Fe_7@NCNS) during high-temperature annealing. Co_3Fe_7@NCNS exhibits exceptional ORR activity (onset potential (E_{onset}) = 0.962 V, half-wave potential ($E_{1/2}$) = 0.869 V) and bifunctional electrocatalytic performance, accompanied by a low reversible overvoltage of 0.82 V. Combining X-ray absorption fine structure (XAFS) spectroscopy and density functional theory (DFT) calculations, we elucidate that the strong interactions between the synthesized Co_3Fe_7@NCNS alloy particles optimize the adsorption energy of oxygen intermediates, thereby playing a crucial role in enhancing catalytic activity. Furthermore, the Co_3Fe_7@NCNS-equipped Zn-air battery demonstrates a higher open-circuit voltage of 1.46 V and remarkable power density of 202.8 mW·cm^{-2}. It also exhibits excellent cycling stability, with a high specific capacity of 779.2 mA·h·g^{-1}, outperforming that of the Pt/C-RuO_2 counterpart.

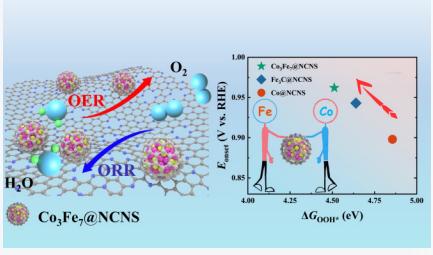

KEYWORDS: bifunctional catalyst, CoFe alloy, Zn-air battery, nitrogen-doped carbon, adsorption energy

1 Introduction

In light of the gradual depletion of traditional energy and the worsening ecological crisis, renewable energy storage and conversion technologies have garnered widespread attention [1]. Zinc-air batteries have the advantages of high energy density (1084 W·h·kg^{-1}), low cost, excellent stability and safety and thus become a new generation of energy storage devices with great application potential [2]. However, the charging and discharging processes of rechargeable metal-air batteries involve two basic electrochemical reactions: the oxygen reduction reaction (ORR) and oxygen evolution reaction (OER) [3, 4]. These two half-reactions involve multi-step proton-coupling and electron transfer processes, resulting in extremely high overpotential due to slow electron transfer kinetics. his severely limits the energy utilization rate and round-trip energy efficiency of rechargeable zinc-air batteries [5]. At present, precious metals such as Pt-based, Ir-based

Received: September 19, 2024; **Revised:** November 6, 2024
Accepted: November 18, 2024

✉Address correspondence to Yuanqing Sun, yqsun@cup.edu.cn; Zhenxing Li, lizx@cup.edu.cn; Yu Wang, wangyu19@westlake.edu.cn; Jian Liu, liujian@cup.edu.cn

and Ru-based materials are widely used in ORR and OER due to their excellent intrinsic activity [6–8]. However, their widespread application is constrained by limited reserves, high prices, poor stability and lack of dual-functional activity [8, 9]. Therefore, the development of a low-cost and stable bifunctional electrocatalyst for Zn-air batteries (ZAB) holds significant value.

Currently, transition metals (Fe, Co, Mn, Ni, etc.) and their derivatives are considered as a class of promising substitutes for noble metal-based catalysts in ZAB [10–14]. In particular, Fe-N-C active centers, represented by iron phthalocyanine, often exhibit superior ORR catalytic performance compared to precious metals under alkaline conditions, owing to the optimal adsorption energy of *OOH and *OH intermediates [15, 16]. Unfortunately, the OER activity displayed by Fe-N-C active sites is not ideal [13] and it has been proved that isolated active sites are prone to decompose or agglomerate prolonged exposure to high potentials [17]. In this regard, such as FeCo, FeMo and FeNi, among others, have been designed and synthesized, demonstrating excellent activity for both ORR and OER under alkaline conditions [18–20]. Compared to a single transition metal component, the unique electron coupling effect between polymetallic components can further promote the catalytic reaction [21, 22]. Among a plethora of alloy catalysts, CoFe alloy has been widely studied due to its strong intrinsic electron regulation ability which can significantly reduce the reaction energy barrier, along with its abundant resource reserve [17, 18]. Su et al. prepared FeCo nanoparticles (NPs) *in-situ* grown on nitrogen-doped graphitic carbon nanotubes with bamboo-like structure. By increasing the introduction of Co, the binding energy of Fe components in the alloy is increasing. It suggests that the strong interaction between Co and Fe causes the electron cloud of the Fe element to shift toward the Co element, thereby regulating the activation ability of the Fe component toward the intermediate state of oxygen [23]. Additionally, Wang [19] and Deng groups [24] also synthesized FeCo bimetallic catalyst. Compared to a single Fe/Co component metal particle, doping with another metal induces changes and rearrangements in the electron cloud of the Fe/Co element. These results further demonstrate the strong coupling effect between Fe/Co, altering its own electronic structure and optimizing the intrinsic activity of FeCo alloy particles [25].

It should also be noted that alloy catalysts still face challenges such as stability issues and susceptibility to self-polymerization, especially during high-potential or high-current electrocatalytic processes [25]. To achieve catalysts with high activity and stability, the confinement of alloy particles on a stable carbon carrier has proven to be a viable approach [26, 27]. The closely bonded carbon coating layer can not only prevent the degradation and agglomeration of alloy particles, thus improving the lifetime of the active sites, but also enhance the electronic conductivity of the catalyst through strong interaction between the carrier and the metal, thereby further enhancing the intrinsic activity of the catalyst. Furthermore, the doping of non-metallic elements, such as N, P and S, can modify the electronic structure of the carbon carrier surface, optimize the adsorption energy of oxygen-containing intermediates during the reaction, reduce the kinetic energy barrier and improve the intrinsic activity of the catalyst active site [28–30]. For example, N has a higher electronegativity (3.04) than C (2.55). This means that the introduction of N will cause leading C to take on a positive charge due to the transfer of electrons from C to N [31]. The positively charged element C exhibits Lewis acidity, which further optimizes the adsorption of oxygenated intermediates [32]. Hao et al. prepared the N,P-codoped carbon (NPC)/FeCo alloy NPs embedded in the N,P-codoped carbon coated nitrogen-doped carbon nanotubes (FeCo@NCNT) through the calcination of the graphene oxide (GO)-coated PS spheres with metal salt and it only needs an overpotential of 339.5 mV (at 10 mA·cm^{-2}) for OER and an onset potential of 0.92 V to actuate ORR [31]. In addition, the N, S co-doped hollow carbon nanocages (FeCo-NS-HNCs) synthesized by Liu's research group exhibited excellent bifunctional catalytic activity, which was attributed to the synergistic coupling of metal sites and N, S co-doping to optimize the adsorption and desorption of metal-nitrogen site (M-N$_x$) [33]. Above all, doping of nonmetallic elements plays a very important role in the modulation of the electronic structure of the catalyst. However, the current approach often involves simply mixing nitrogen-containing organic compounds with iron-cobalt elements, followed by high-temperature annealing to obtain CoFe@C catalysts. Yet, this synthesis process suffers from poor controllability and uniformity [26]. Moreover, directly using carbon carriers to reduce metal salts can disrupt the structure of the carbon matrix's non-metallic heteroatoms, while the defect sites may sharply decrease due to metal occupation and secondary carbonization [3, 34]. Therefore, there is a pressing need for further optimization of the synthesis process for CoFe@C catalysts.

In this study, we have designed a strategy for the preparation of a kind of high-performance oxygen electrode catalyst consisting of CoFe alloy NPs embedded in nitrogen-doped ultra-thin carbon nanosheets (Co_3Fe_7@NCNS). Co_3Fe_7@NCNS exhibits excellent ORR catalytic capability (onset potential (E_{onset}) = 0.962 V, half-wave potential ($E_{1/2}$) = 0.869 V), which is superior to the single-phase metal catalysts, as well as very high stability and methanol resistance. At the same time, the Co_3Fe_7@NCNS catalyst appeared outstanding bifunctional activity with a reversible overvoltage (ΔE) value of 0.82 V. What is more, the ZAB equipped with Co_3Fe_7@NCNS possessed a higher open-circuit voltage (1.46 V) and a remarkable power density of 202.8 mW·cm^{-2}, as well as excellent cycling stability compared to the Pt/C-RuO_2 cell. Its outstanding activity is attributed to the bidirectional redox reaction between CoFe layered double hydroxide (CoFe LDH) and NCNS during the synthesis of Co_3Fe_7@NCNS. While obtaining CoFe alloy particles with excellent intrinsic activity, the specific surface area of NCNS further increased to 381.15 m^2·g^{-1}. X-ray absorption fine structure (XAFS) and density functional theory (DFT) calculations revealed that the strong interaction between Fe and Co optimized the adsorption capacity of *OOH intermediates, thereby enhancing the ORR catalytic capability.

2 Experimental

2.1 Synthesis of ultra-thin NCNS

The synthesis of ultra-thin nitrogen-doped carbon nanosheets (NCNS) were achieved through thermal decomposition using a soft template sacrificial method. In simple terms, a certain amount of melamine and glucose (melamine to glucose ratio: 30:1) were fully mixed using a ball mill. The white powder was then placed in a porcelain boat, followed by heating up to 600 °C at a rate of 2 °C·min^{-1} and keeping for 1 h, then further heating up to 900 °C for another 1 h in Ar-saturated circumstance. After cooling to room temperature, NCNS was obtained for future applications.

2.2 Synthesis of Co_3Fe_7@NCNS

Typically, the CoFe LDH@NCNS precursor were synthesized through asimple hydrothermal process. 10 mg of $Fe(NO_3)_3·9H_2O$ and $Co(NO_3)_2·6H_2O$ (with a Fe/Co feed mass ratio of 2:1) were dissolved in 10 mL of deionized water which contained 150 mg urea and 46.5 mg NH_4F with stirred for 2 h. Subsequently, 10 mg of NCNS were added to the uniform solution, which was subsequently sonicated for 2 h to achieve a homogeneous dispersion. The dispersion was then transferred to a hydrothermal reactor and heated to 120 ℃, maintaining this temperature for 8 h. The obtained CoFe LDH@NCNS was washed three times with deionized water and ethanol before being dried in a 45 ℃ oven. Finally, CoFe LDH@NCNS was placed in a porcelain boat and heated to 900 ℃ at 10 ℃·min^{-1} for 2 h under an argon atmosphere. The target catalyst Co_3Fe_7@NCNS was obtained after cooling to room temperature. Additionally, in order to explore the influence of different annealing temperatures on the catalyst, the annealing treatments were carried out at 600, 700, 800 and 1000 ℃, named as Co_3Fe_7@NCNS-600 ℃, Co_3Fe_7@NCNS-700 ℃, Co_3Fe_7@NCNS-800 ℃ and Co_3Fe_7@NCNS-1000 ℃, respectively.

2.3 Synthesis of Co@NCNS and Fe_3C@NCNS

In the aforementioned hydrothermal process, only $Fe(NO_3)_3·9H_2O$ and $Co(NO_3)_2·6H_2O$ metal salts were added respectively, while the rest of the synthesis procedure remained unchanged. The resulting black powder samples were designated as Fe_3C@NCNS-900 ℃ and Co@NCNS-900 ℃ respectively.

3 Results and discussion

3.1 Structural and morphological characterizations

Co_3Fe_7@NCNS electrode was fabricated by combining hydrothermal method and annealing carbonization process, as depicted in Fig. 1. Initially, NCNS were obtained by high-temperature carbonization of thoroughly mixed uniform melamine and glucose powders under argon. Subsequently, the Fe and Co precursors were converted into regular hexagonal CoFe LDH loaded on NCNS under the action of urea and ammonium fluoride through hydrothermal action [35]. Following pyrolysis, the CoFe LDH underwent successfully reduced into CoFe alloy nanoparticles encapsulated in a sprinkling of carbon layers. The synthesis mechanism for the Co_3Fe_7@NCNS catalyst was hypothesized based on previous literature and structural characterization analysis. During the carrier synthesis process, melamine underwent decomposition and conversion into a significant amount of graphitic carbon nitride (g-C_3N_4) at approximately 600 ℃ [36]. In the process of pyrolysis, as the temperature further increases, g-C_3N_4 spontaneously decomposes into gaseous CN_x molecule, which serves as self-sacrificial templates to peel off the ultra-thin carbon layer [37]. This strategy enabled the simultaneous capture of nitrogen elements by the carbon skeleton, resulting in the formation of ultra-thin nitrogen-doped carbon nanosheets.

As revealed by scanning electron microscopy (SEM) in Fig. S1(a) in the Electronic Supplementary Material (ESM), the obtained nitrogen-doped carbon material exhibits a stacked layered structure due to the decomposition of g-C_3N_4 intercalation. It can be seen from the transmission electron microscopy (TEM) of NCNS (Fig. S1(b) in the ESM) that the carbon material exhibits the characteristics of ultra-thin carbon nanosheets. The synthesis of CoFe LDH (Figs. S2(a) and S2(b) in the ESM) on the NCNS substrate was obtained via a traditional hydrothermal process, where Co and Fe precursors were grown under the combined action of urea and ammonium fluoride to obtain hexagonal LDH nanosheets. It stands to reason that a higher Fe precursor feed ratio would engender the coexistence of CoFe LDH and FeOOH (Figs. S2(c) and S2(d) in the ESM). Subsequent high-temperature annealing facilitated the reduction of CoFe LDH to form CoFe alloy NPs, serving as optimal active sites.

The microstructure of Co_3Fe_7@NCNS was further characterized by SEM and TEM. As shown in Fig. 2(a), the nitrogen-doped carbon layer loaded with CoFe alloy NPs still maintain its lamellar shape accompanied by the disappearance of hydroxyl groups oxides. The resultant Co_3Fe_7@NCNS electrocatalyst, depicted in Fig. 2(b), exhibits a uniform distribution across the substrate. High-resolution TEM (HRTEM) image (Fig. 2(c)) confirms that the lattice fringes of the metal nanoparticles are measured to be 0.202 nm, corresponding to the 110 lattice plane of the Co_3Fe_7 alloy phase. Notably, the CoFe alloy particles are discernibly enveloped within multiple layers of graphitic carbon shells. As reported in Refs. [38, 39], CoFe nanoparticles exert a profound influence on the surrounding carbon layer. Electrons emitted from the CoFe alloy particles are transferred to the encapsulated carbon layer, thereby reducing its local work function. And the selected area electron diffraction (SAED, Fig. 2(d)) of the alloy crystal grains the formation of polycrystalline Co_3Fe_7 during annealing under argon conditions. The high angle annular dark-field-scanning TEM (HAADF-STEM) image and elemental mappings (Fig. 2(e)) show that C, N and O elements are evenly distributed throughout the sheet. Crucially, the overlapping distribution of Co and Fe elements

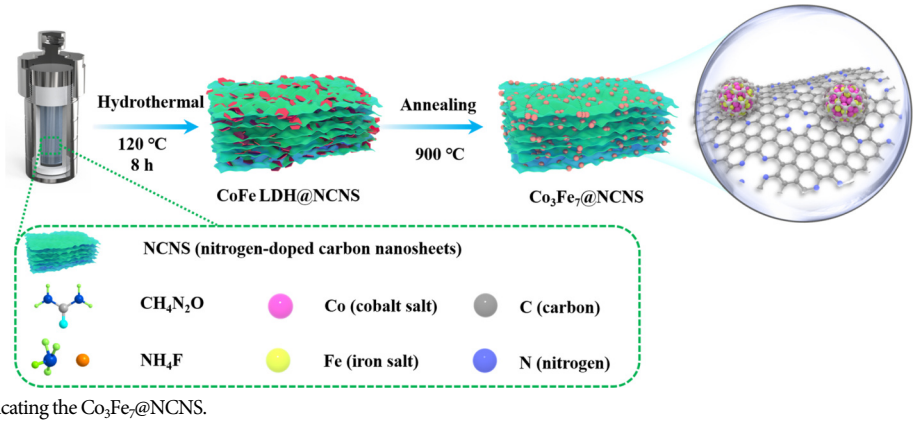

Figure 1 Scheme for fabricating the Co_3Fe_7@NCNS.

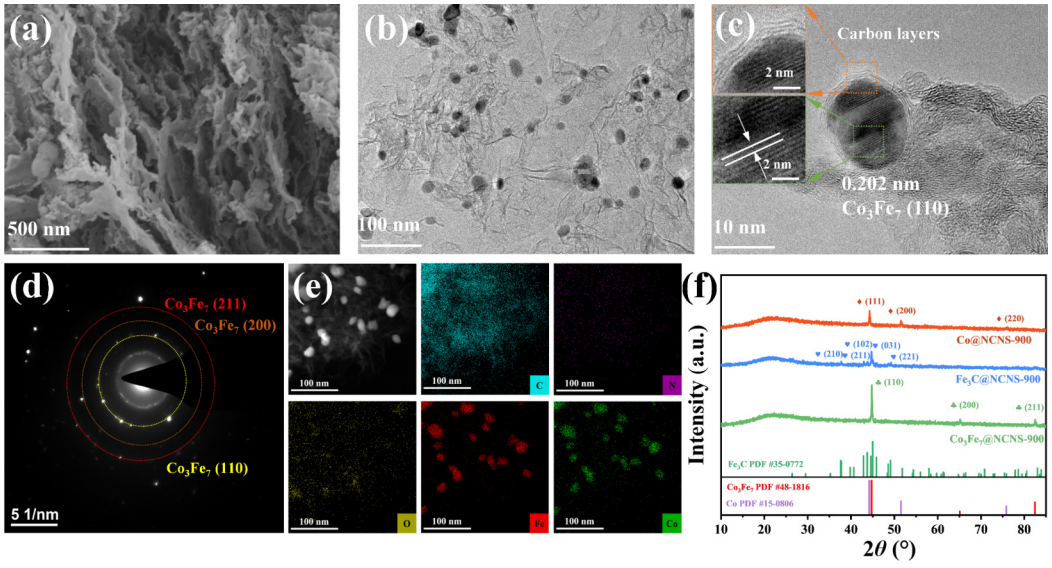

Figure 2 (a) SEM and (b) TEM images of Co_3Fe_7@NCNS. (c) HRTEM images of a metal particle wrapped in the carbon layers. (d) The SAED pattern of an alloy nanoparticles. (e) HAADF-STEM image and corresponding elemental mappings of Co_3Fe_7@NCNS. (f) XRD patterns of Co_3Fe_7@NCNS, Co@NCNS-900 and Fe_3C@NCNS-900.

corroborates the elemental composition of the metal nanoparticles. This means that there are effective links between metal elements (Co, Fe) and non-metal elements (C, N), resulting in more C-M and N-M active sites to promote catalytic ability. In addition, the elements Fe, Co, C, N and O coexist in the typical sample, as confirmed by energy dispersive X-ray spectroscopy (EDS) analysis (Fig. S3 in the ESM). The mass and atomic percentages of these elements were utilized to estimate the approximate content of each component in Co_3Fe_7@NCNS. It is notable that the atomic ratio of cobalt to iron, as determined by EDS analysis, is approximately 0.55. This finding is supported by subsequent X-ray diffraction (XRD) results.

Powder XRD characterization (Fig. 2(f) and Fig. S4 in the ESM) of Co_3Fe_7@NCNS and four comparative samples (pure Co@NCNS-900, Fe_3C@NCNS, Co_3Fe_7@NCNS-1, Co_3Fe_7@NCNS-3) delineated the crystal structure variations. The three main diffraction peaks at 44.7°, 65.1°, 82.4° for Co_3Fe_7@NCNS correspond to the (110), (200), (211) planes of Co_3Fe_7 (PDF #48-1816). The metal NPs formed with different Fe and Co feeding ratios all belong to Co_3Fe_7 alloy nanoparticles, corresponding to which they produce the same diffraction peak. Notably, at a 2:1 input mass ratio (Fe:Co), CoFe LDH assumes the most pronounced crystal morphology, manifesting as superior active sites during the annealing reduction process (Fig. S4 in the ESM). Conversely, introduction of solely Fe or Co metal salts results in the generation of corresponding nanocapsules or nanorod compounds, respectively, as depicted in SEM (Figs. S5(a)–S5(c) in the ESM) and TEM (Figs. S5(b)–S5(d) in the ESM) images. XRD patterns (Fig. S6 in the ESM) for singular cobalt or iron salts demonstrate the formation of iron oxyhydroxide or cobalt trioxide, respectively. After annealing, TEM (Fig. S7 in the ESM) was conducted to characterize the synthesized Co@NCNS-900 and Fe_3C@NCNS-900 catalysts. The HRTEM images (inset of Figs. S7(b) and S7(d) in the ESM) imply an inter-fringe distance of 0.204 and 0.201 nm, corresponding to the (111) plane of Co and (031) plane of Fe_3C, respectively. The XRD pattern of Co@NCNS-900 reveals the presence of pure crystalline metallic cobalt (PDF #15-0806), while the XRD pattern of Fe_3C@NCNS-900 confirms the crystalline nature of Fe_3C metal NPs in Fig. 2(f). This evidence supports the formation of the CoFe alloy phase during the annealing process, which is a consequence of the interaction between Fe and Co. Additionally, all synthesized samples display a characteristic broad diffraction peak centered around 21.5°, which is attributed to the presence of amorphous carbon derived from aromatic carbon sheets.

To delve deeper into the influence of pyrolysis temperature on alloy particle formation and ORR electrocatalytic performance, a series of Co_3Fe_7@NCNS-T catalysts were synthesized across a spectrum of annealing temperatures (600–1000 °C). As delineated in Fig. S8 in the ESM, all specimens exclusively exhibit diffraction peaks characteristic of CoFe alloys, devoid of any LDH or oxyhydroxide signatures. These findings underscore the complete reduction of CoFe LDH to CoFe alloy at 600 °C, with peak intensity steadily escalating as temperatures ascend to 900 °C, indicative of augmented alloygrowth and crystallinity refinement. To scrutinize the transformational impact from CoFe LDH crystals to CoFe alloy phase on the carbon substrate during annealing, N_2 adsorption/desorption isotherms were performed. As illustrated in Fig. S9(a) in the ESM, the Brunauer–Emmett–Teller (BET) analysis demonstrate a typical type IV plot with a hysteresis loop, indicating the formation of a substantial number of mesoporous structures [40]. It is noteworthy that the BET surface area of Co_3Fe_7@NCNS (381.15 $m^2 \cdot g^{-1}$) exceeds that of CoFe LDH@NCNS (256.79 $m^2 \cdot g^{-1}$) and NCNS (365.41 $m^2 \cdot g^{-1}$). The pore size distribution (Fig. S9(b) in the ESM) is predominantly comprised of micropores and mesopores, with the Co_3Fe_7@NCNS produced after pyrolysis exhibiting a greater propensity for the formation of mesoporous structures. This observation suggests that during high-temperature reduction process, the carbon matrix also undergoes local oxidation and dissociation to generate more mesopores during the reduction of CoFe LDH. The degree of graphite defects in carbon materials is typically gauged from the Raman spectrum, by comparing the intensity ratios of defective sp^3 carbon (D band) at 1348 cm^{-1} to graphite sp^2 carbon (G band) at 1589 cm^{-1} in the Raman spectra [41]. As illustrated in Fig. S9(c) in the ESM, the calculated Co_3Fe_7@NCNS peak intensity ratio of 1.12 exceeds that of FeCo LDH@NCNS (0.98) and NCNS (1.04). The higher Co_3Fe_7@NCNS

I_D/I_G ratio (I_D/I_G: peak intensity ratio of D band and G band) reflects that the nitrogen-doped carbon layer produces more defective sites. Essentially, an abundance of unsaturated carbon defects, expansive surface area and copious mesoporous structures afford a plethora of active sites, enhancing electrolyte and dissolved oxygen mass transfer and diffusion, thereby underpinning their catalytic prowess in ORR/OER reactions [42].

The elemental composition and chemical valence state of the Co_3Fe_7@NCNS were elucidated via X-ray photoelectron spectroscopy (XPS) analysis. It can be obtained from the full spectrum (Fig. S10(a) in the ESM) that the surface element composition of the Co_3Fe_7@NCNS catalyst includes C 1s (285 eV, 86.79%), O 1s (532 eV, 6.62%), N 1s (400 eV, 5.74%), Fe 2p (711 eV, 0.66%) and Co 2p (785 eV, 0.19%). The formation and type of CoFe alloy species can also be confirmed from the XPS semi-quantitative analysis results. As shown in Fig. S10(b) in the ESM, the C 1s spectrum in Co_3Fe_7@NCNS is deconvoluted into three carbon species, attributed to C–C/C=C (284.8 eV), C–N/O (285.6 eV) and O–C=O (290.1 eV) respectively [43]. Concurrently, the high-resolution N 1s spectrum (Fig. S10(c) in the ESM) of Co_3Fe_7@NCNS can be divided into five separate peaks at 398.1, 399.5, 400.6, 401.7 and 404.2 eV, which are attributed to pyridine nitrogen, M–N, pyrrole nitrogen, graphitic nitrogen and nitrogen oxide respectively, other comparison samples are similar (Figs. S10(d)–S10(i) in the ESM) [44]. The split-peak fitting of the N 1s spectrum demonstrated that the metal on the surface of the catalyst coordinates with N to form M-N_x sites, which modulate the electronic structure with pyridine nitrogen and pyrrole nitrogen, thereby promoting the adsorption of oxygen molecules [45]. Furthermore, graphitic nitrogen enhances catalyst conductivity and accelerates electron transfer. The percentage distributions (Fig. S11 in the ESM) of nitrogen species obtained by integrating the fine spectra of the corresponding N species indicate that various nitrogen species are present in Co_3Fe_7@NCNS in a uniform manner. The synergistic effect among these species jointly promotes the ORR/OER process.

In the Fe 2p fine spectrum (Fig. 3(a)), four distinct binding energy peaks at 711.10, 724.07, 714.80 and 727.60 eV correspond to Fe^{2+} $2p_{3/2}$, Fe^{2+} $2p_{1/2}$, Fe^{3+} $2p_{3/2}$ and Fe^{3+} $2p_{3/2}$, respectively [46]. It is proposed that the higher valence states of Fe can be considered to be Fe-N_x/O_y unit points, formed by coordination with surface N and O, combined with the absence of metal oxides in XRD. Furthermore, the signals observed at 707.40 and 720.71 eV are believed to be indicative of metallic Fe^0, accompanied by satellite

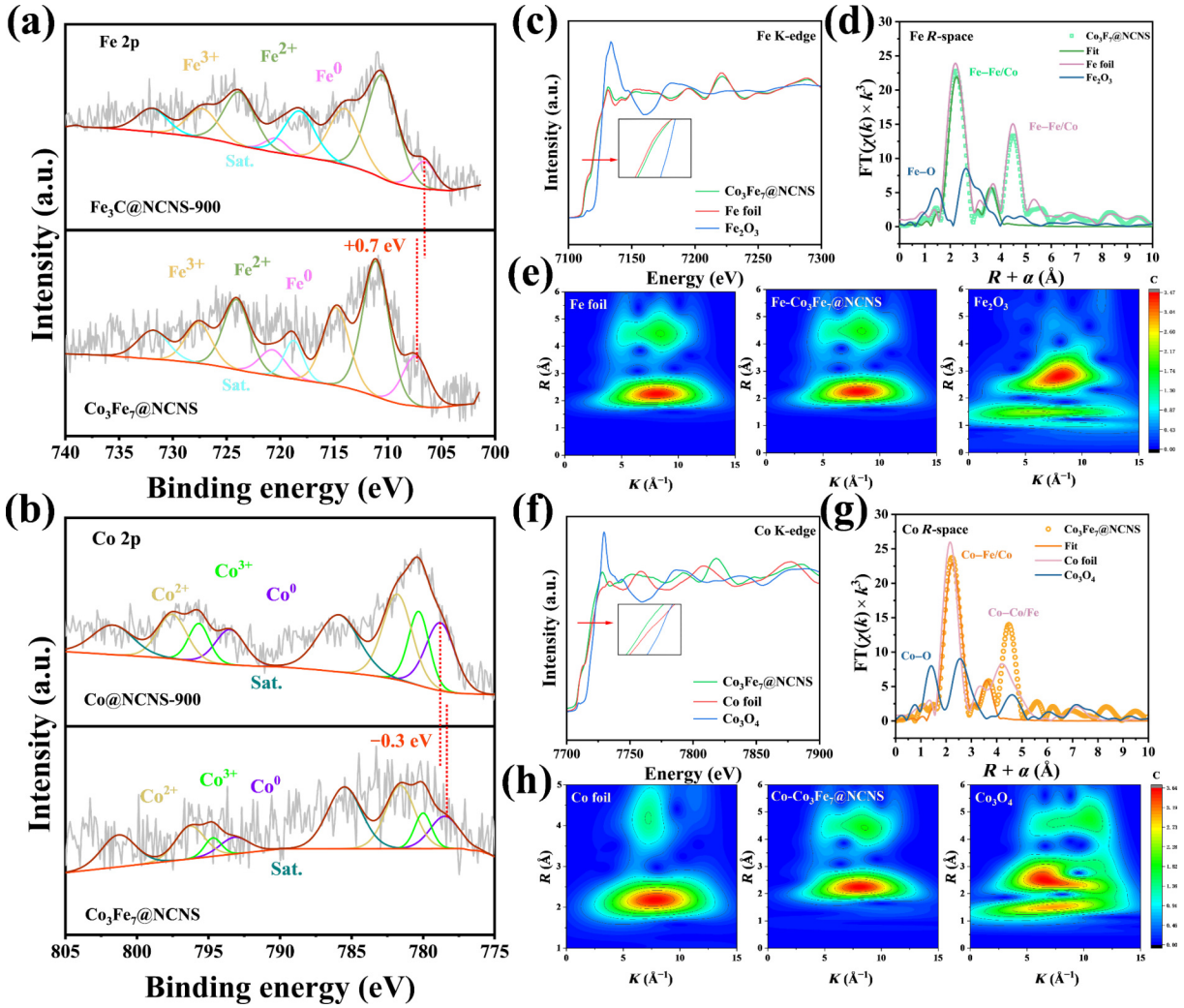

Figure 3 (a) High-resolution XPS spectra of Fe 2p of Co_3Fe_7@NCNS and Fe_3C@NCNS-900. (b) High-resolution XPS spectra of Co 2p of Co_3Fe_7@NCNS and Co@NCNS-900. (c) XANES spectra of the Fe K-edge. (d) Fourier transform of the EXAFS spectra in *R*-space of Fe K and (e) wave transform-EXAFS. (f) XANES spectra of the Co K-edge. (g) Fourier transform of the EXAFS spectra in *R*-space of Co K and (h) wave transform-EXAFS.

peaks at 718.75 and 731.85 eV. Similarly, the Co 2p fine spectrum (Fig. 3(b)) shows Co^{2+} $2p_{3/2}$, Co^{2+} $p_{1/2}$, Co^{3+} $2p_{3/2}$ and Co^{3+} $2p_{3/2}$, located at 781.60, 796.29, 780.00 and 794.69 eV respectively. High-value Co is also considered to be the generation of Co-N_x/O_y species. The Co 2p spectrum also reflects the generation of zero-valent Co (778.50 and 793.19 eV) accompanied by satellite peaks (785.50 and 801.29 eV). The coexistence of metallic Fe^0 and metallic Co^0 proves the generation of CoFe alloy once again, which can be combined with the TEM and XRD results to confirme each other. It is worth noting that compared to the Fe 2p spectrum of Fe_3C@NCNS and the Co 2p spectrum of Co@NCNS, the binding energy position of the Fe element is shifted to the high energy position by about 0.7 eV, while the binding energy of the Co element is shifted toward the low binding position by about 0.3 eV. It well confirms the strong interaction between Co and Fe in the CoFe alloy and the electrons shift from low electronegativity Fe to high electronegativity Co [47].

X-ray absorption near-edge structure (XANES) spectroscopy was employed to further investigate the electronic structures of Fe and Co elements and their corresponding coordination environments. As shown in Fig. 3(c), it is evident that the XAFS curve of Co_3Fe_7@NCNS exhibits a trend similar to that of Fe foil, contrasting with the spectrum of Fe_2O_3. However, the XANES curve of Co_3Fe_7@NCNS shows a slight shift towards higher energy, indicating a slight positive charge on iron atoms within the alloy particles. Moreover, the wavelet-transformed spectra (Fig. 3(e)) distinctly demonstrate the close resemblance of iron atoms in Co_3Fe_7@NCNS to those in Fe foil. Furthermore, Fourier-transformed extended XAFS (FT-EXAFS, Fig. 3(d)) spectra in *R*-space reveal that the coordinating atoms of Fe in Co_3Fe_7@NCNS are predominantly Fe and Co. Similar results were obtained from Co K-edge XANES (Fig. 3(f)) spectra and FT-EXAFS spectra (Fig. 3(g)). Combined with the wavelet-transformed spectra (Fig. 3(h)), the existence of Co^0 is also proved. The oxidation state of cobalt atoms in Co_3Fe_7@NCNS is in basic agreement with that of Co foil, with coordinating atoms being Fe and Co. It is noteworthy that the Co K-edge XANES curve of Co_3Fe_7@NCNS exhibits a slight shift towards lower energy, suggesting a slight negative charge on cobalt atoms within the alloy particles. Upon comprehensive analysis, it is convincingly attested that Fe and Co elements in the Co_3Fe_7@NCNS catalyst exist in the form of alloy NPs, with Co-Fe elements exhibiting extremely strong interactions. The observed electron flow from Fe to Co is consistent with XPS analysis. Corresponding EXAFS *k*-space fitting curves are presented in the Tables S1 and S2 and Fig. S12 in the ESM. The results of Bader charge calculation (Fig. S13 and Table S3 in the ESM) indicate that the valence electron count for Fe atoms is approximately 7.8, while that for Co atoms is around 9.2. In comparison to the reference valence electron counts of Fe (8) and Co (9), it is evident that in the CoFe alloy, Fe element functions as an electron donor and Co element serve as an electron acceptor. As evidenced by the differential charge density analysis (Fig. S14 in the ESM), notable disparities in charge offsets of Fe and Co elements further substantiate the robust interaction between alloy particles and the graphitic carbon layer, thereby substantially enhancing intermediate adsorption capacity during ORR/OER processes and ultimately improving catalyst activity.

3.2 Electrocatalytic performance evaluation

In light of the aforementioned pertinent characterisations, the electrocatalytic activity for ORR of the synthesized catalysts was tested by a typical three-electrode system in 0.1 M O_2-saturated KOH solvent. First, the annealing temperature of the catalyst was optimized through ORR testing on rotating disk electrode (RDE) and the results are shown in Figs. S15 and S16 in the ESM, where the obtained Co_3Fe_7@NCNS showed the best ORR activity at a pyrolysis temperature of 900 °C. It can be observed that the activity of the catalyst Co_3Fe_7@NCNS-*T* (*T*: annealing temperature) continues to increase from 600 to 900 °C, until the catalyst activity significantly deteriorates when the temperature reaches 1000 °C. Such an activity change trend corresponds to the above XRD (Fig. S7 in the ESM), proving that CoFe alloy particles with good crystallinity are the main active sites. Therefore, the samples tested next were all obtained at 900 °C treatment. For comparison, the ORR electrocatalytic activity of commercial Pt/C (20 wt.%) catalyst was also tested.

In the typical cyclic voltammetry (CV) curves presented in Fig. 4(a), all tested samples showed no obvious characteristic peaks in N_2-saturated 0.1 M KOH solvent. However, clear reduction peaks were observed in O_2-saturated solvents in KOH solvent, indicating that the synthesized catalysts were self-stable and exhibited ORR activity. Co_3Fe_7@NCNS emerges a cathodic peak at about 0.854 V which is closest to commercial Pt/C (0.858 V vs. reversible hydrogen electrode (RHE)), more positive than that of CoFe LDH@NCNS (0.804 V), Co@NCNS (0.819 V) and Fe_3C@NCNS (0.831 V). ORR catalytic activity was further studied using linear sweep voltammetry (LSV) to determine E_{onset}, half-wave potential ($E_{1/2}$) and limiting current density (J_L) at a rotation speed of 1600 rpm in O_2-saturated 0.1 M KOH. As showed in Fig. 4(b), CoFe LDH without annealing treatment exhibited the weakest ORR catalytic activity with the E_{onset} and $E_{1/2}$ at 0.824 and 0.788 V, suggesting a lack of active sites when only supporting hydroxyl oxidation nitrogen-doped carbon support. The catalytic activities were enhanced relative to metal oxides after pyrolytic reduction to metal NPs, even when only Co and Fe are supported on NCNS (Co@NCNS and Fe_3C@NCNS) respectively. Most notably, Co_3Fe_7@NCNS display the highest E_{onset} (0.962 V) and $E_{1/2}$ (0.869 V) at elevated temperatures when CoFe LDH was reduced to carbon shell-encapsulated CoFe alloy NPs. Compared with Co@NCNS-900 (E_{onset} = 0.898 V, $E_{1/2}$ = 0.836 V) and Fe_3C@NCNS-900 (E_{onset} = 0.943 V, $E_{1/2}$ = 0.855 V), it is evident that the formation of alloy is greatly enhanced the catalytic activity of ORR. Moreover, Co_3Fe_7@NCNS exhibits excellent activity that is only slightly weaker than the commercial noble metal Pt/C catalyst (E_{onset} = 0.991 V, $E_{1/2}$ = 0.861 V) and Co_3Fe_7@NCNS possesses the largest limiting current density (J_L = 5.49 mA·cm^{-2}) under the same test conditions. In order to further explore the impact of different Fe/Co feed ratios on the catalyst activity, as shown in Figs. S17 and S18 in the ESM, Co_3Fe_7@NCNS showed the best ORR activity. Combined with the XRD pattern analysis (Fig. S4 in the ESM), it can be speculated that only when the feed ratio of Fe/Co is 2:1, the obtained CoFe alloy phase can form the Co_3Fe_7 alloy phase with the best crystallinity, which is very crucial in this catalytic system. The E_{onset} and $E_{1/2}$ of the catalysts mentioned above are unified in Fig. 4(c).

In addition, the Tafel slope of the obtained samples were converted from the corresponding ORR polarization curve at 1600 rpm in Fig. 4(d). Co_3Fe_7@NCNS reveals the smallest Tafel slope (66.58 mV·dec^{-1}) compared to other catalysts (CoFe LDH@NCNS-96.13 mV·dec^{-1}, Co@NCNS-900-73.41 mV·dec^{-1} and Fe_3C@NCNS-900-69.9 mV·dec^{-1}) and almost reaching the level of Pt/C (65.70 mV·dec^{-1}). This indicates the rapid catalytic reaction

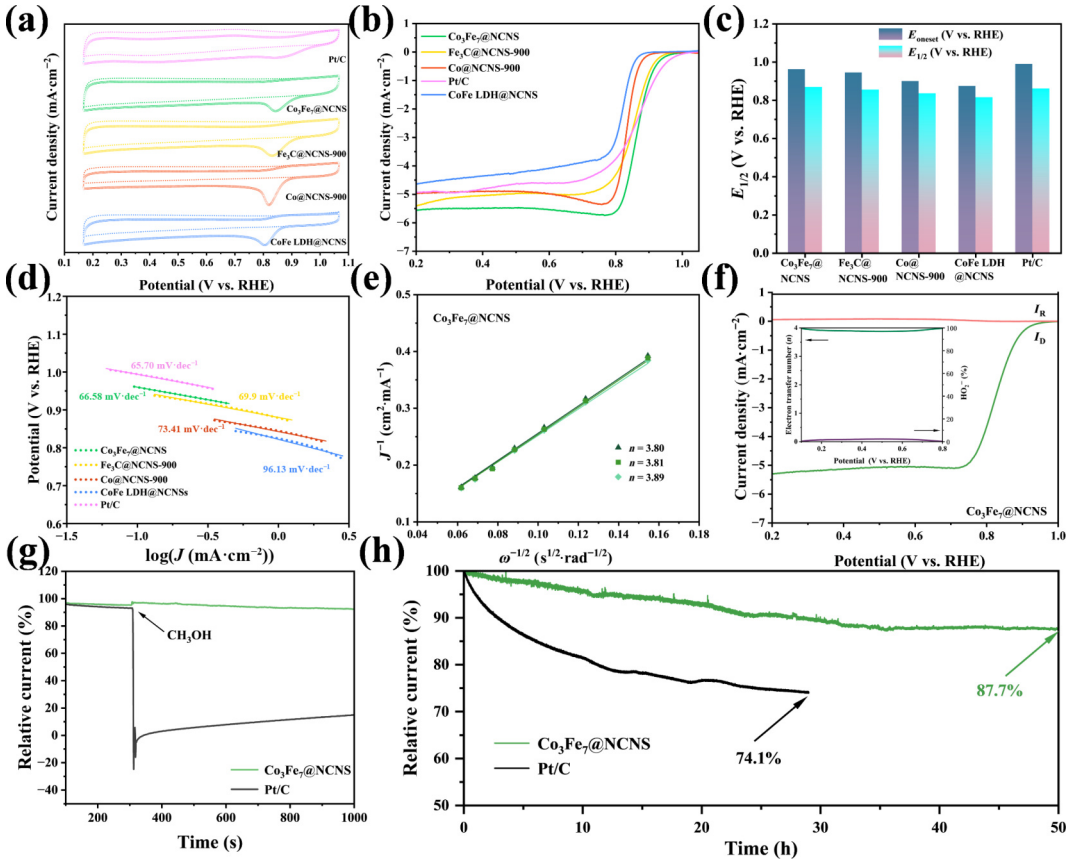

Figure 4 (a) CV curves of the investigated catalysts in N_2- and O_2- saturated 0.1 M KOH electrolyte at a sweep speed of 20 mV·s^{-1}. (b) LSV curves in the O_2-saturated 0.1 M KOH solution at a rotation rate of 1600 rpm. (c) E_{onset} and $E_{1/2}$ of obtained catalysts. (d) Corresponding Tafel plots. (e) The K–L plots converted from the LSV curve at different rotation rates. (f) RRDE polarization curves and the inset is the electron transfer numbers and yields of peroxide obtained from RRDE. (g) Chronoamperometric responses of Co_3Fe_7@NCNS and Pt/C (20 wt.%) upon addition of 3 M methanol. (h) Chronoamperometric responses of Co_3Fe_7@NCNS and Pt/C (20 wt.%) at 1200 rpm for 50 h.

kinetics of the Co_3Fe_7@NCNS catalyst, highlighting its superior performance in facilitating the oxygen reduction reaction. Meanwhile, the electrochemical impedance spectroscopy (EIS) results for Co_3Fe_7@NCNS (Fig. S19 in the ESM) display the smallest semicircle diameter in the high frequency region, indicating an enhancement in charge transfer. Additionally, the largest slope observed in the low frequency region demonstrates the fastest ion diffusion rate [48]. Further investigation into the ORR reaction kinetics of the Co_3Fe_7@NCNS catalyst, the polarization curves with different rotation speeds from 400 to 2500 were tested in Fig. S22(a) in the ESM. The Koutecky–Levich (K–L) plots (Fig. 4(e)) converted from the LSV curve show good linearity at different potentials, which means that the linear relationship represents the first-order reaction kinetics at the same dissolved oxygen level. Furthermore, it exhibits a constant electron transfer number (3.8–3.9) within a certain voltage range. At the same time, the electron transfer numbers of the Fe_3C@NCNS-900, Co@NCNS-900 and CoFe LDH@NCNS were estimated to be 3.5–3.7, 3.6–3.7, 3.4–3.5, respectively, signifying strong differences between Co_3Fe_7@NCNS catalysts (Fig. S20 in the ESM). This distinctive behavior underscoring its unique ability to modulate intermediate adsorption and optimize the reaction process for enhanced selectivity towards the four-electron reaction pathway. The rotating ring-disk electrode (RRDE) test of Co_3Fe_7@NCNS was performed at 1600 rpm and the results are shown in Fig. 4(f), the n value measured over the potential range of 0.2–0.8 V is approximately 3.9 as same as the K–L equation based on the RDE tests, which further confirmed the efficient four-electron catalytic process of Co_3Fe_7@NCNS. And the H_2O_2 yield for Co_3Fe_7@NCNS had remained below 3% at the potential ranging from 0.2 to 0.8 V.

To further investigate the reasons for the optimal catalytic capacity of the Co_3Fe_7@NCNS ORR, double-layer capacitance (C_{dl}) is one of the important parameters for its linear correlation with electrochemical active surface area (ECSA). The CV curves are obtained by cyclic voltammetry test and the voltage range is from 0.99–1.09 (Fig. S21 in the ESM). According to Fig. S22(b) in the ESM, it is obvious that Co_3Fe_7@NCNS displays the highest C_{dl} (15.74 mF·cm^{-2}) compared to Fe_3C@NCNS-900 (12.26 mF·cm^{-2}). Co@NCNS-900 (13.26 mF·cm^{-2}) and CoFe LDH@NCNS (14.99 mF·cm^{-2}), indicating the enlarged active area of the Co_3Fe_7@NCNS. Interestingly, CoFe LDH@NCNS exhibits the closest C_{dl} to Co_3Fe_7@NCNS, implying that the CoFe LDH with ORR catalytic inertness was seamlessly transformed into the highly active CoFe alloy during the annealing process. The above analysis proves that the excellent ORR activity of the Co_3Fe_7@NCNS catalyst is attributed to the rich catalytic sites provided by its unique nitrogen-doped layered structure and the strong synergistic interaction between metals that optimizes its intrinsic activity.

The utilization of Co_3Fe_7@NCNS as a cathode material in ZAB involves correlating its charge and discharge processes to the OER and ORR activities of the material, respectively. Therefore, the OER catalytic activity of the synthesized catalyst was also studied by LSV

test in N_2-saturated 0.1 M KOH solution. As shown in Fig. S22(c) in the ESM, Co_3Fe_7@NCNS shows a lower overpotential (550 mV) at current density up to 10 mA·cm^{-2} compared to Co@NCNS-900 and Fe_3C@NCNS-900, which are closest to commercial RuO_2 (412 mV). Similarly, the Co_3Fe_7@NCNS electrode exhibits the lowest charge transfer resistance among the all tested electrodes, approaching that of commercial RuO_2 (Fig. S23 in the ESM). This suggests an enhancement in both the conductivity and electron transfer rate of the Co_3Fe_7@NCNS electrode [49]. Furthermore, Co_3Fe_7@NCNS has a superior ΔE of 0.82 V between the ORR and ORR compared to Co@NCNS-900 and Fe_3C@NCNS-900, highlighting the exceptional bifunctional catalytic performance of Co_3Fe_7@NCNS as for the ORR/OER process (Fig. S22(d) in the ESM). The stability and the resistance to methanol are crucial for its prospective application of the catalyst in ZAB. The methanol tolerance of the Co_3Fe_7@NCNS and commercial Pt/C was assessed through chronopotentiometry test method in O_2-saturated 0.1 M KOH and electrolyte solution was accompanied by the injection of 3 M methanol. As illustrated in Fig. 4(g), the commercial Pt/C catalyst showed noticeable attenuation after the introduction of methanol within 300 s. In contrast, the current density of Co_3Fe_7@NCNS remained relatively stable with minor fluctuations, indicating its enhanced resistance to methanol compared to Pt/C. Similarly, long-term chronopotentiometry test was conducted to evaluate the stability of Co_3Fe_7@NCNS and Pt/C in the ORR process. Figure 4(h) displays the normalized *i*–*t* curve tested at 0.8 V (RDE, 1200 rpm), the Co_3Fe_7@NCNS retains 91.7% of its initial current, while Pt/C decays to 74.1% of its initial voltage for up to 28 h. Figure S24 in the ESM illustrates that at a current density of 10 mA·cm^{-2} for OER, the potential undergoes a change of 61 mV after 4000 cycles, which is comparable to the decay rate of commercial RuO_2 activity. This suggests that the Co_3Fe_7@NCNS catalyst exhibits favorable stability. Furthermore, the SEM and TEM of Co_3Fe_7@NCNS were employed to assess the structural stability following a 10-h reaction at a constant potential of 0.85 V. Figures S25(a) and S25(b) in the ESM indicate that the catalyst maintains a distinct carbon layer structure after prolonged operation, showing no significant collapse or dissolution. Additionally, Figs. S25(c) and S25(d) in the ESM demonstrate that the NPs aggregates did not experience dissolution or agglomeration, suggesting that the carbon layer surrounding the metal particles plays a crucial role in maintaining stability during the reaction.

3.3 ZAB performance

These results underscore the robust stability and superior performance of Co_3Fe_7@NCNS as a catalyst for both ORR and OER processes, positioning it as a promising candidate for ZAB applications. As depicted in Fig. S26 in the ESM, a charge–discharge ZAB was assembled by using Co_3Fe_7@NCNS as the air cathode, zinc sheet as the anode and 6 M KOH with 0.2 M $Zn(CH_3COO)_2$ as the electrolyte. For comparison, Pt/C-RuO_2 (with a Pt/C (20 wt.%) and RuO_2 (mass ratio of 1:1) were used in another cell. The open-circuit voltage of the ZAB loaded with Co_3Fe_7@NCNS is 1.46 V, higher than that of the Pt/C-RuO_2-based battery (1.42 V) and closer to the theoretical voltage of 1.65 V of the ZAB (Fig. 5(a)). Figure 5(b) illustrates the discharge polarization curves and charge polarization curves of the ZAB. Obviously, the Co_3Fe_7@NCNS-equipped ZAB exhibits a smaller charge/discharge voltage gap relative to Pt/C-RuO_2 at the same current density, clearly confirming its improved rechargeability. Furthermore, the discharge polarization curves and corresponding energy density curves (Fig. 5(c)) show that the Co_3Fe_7@NCNS-equipped ZAB achieves a higher discharge potential and a maximum energy density of 202.8 mW·cm^{-2}, significantly surpassing the Pt/C-RuO_2 counterpart (142.5 mW·cm^{-2}). Moreover, as expressed in Fig. 5(d), the ZAB with Co_3Fe_7@NCNS also presents a higher specific capacity of 779.2 mA·h·g^{-1} (normalized to the mass of the consumed Zn) than that of the Pt/C-RuO_2-based cell at current densities of 5 mA·cm^{-2}. And the long-term cycling stability of ZAB was evaluated by galvanostatic charge/discharge at current density

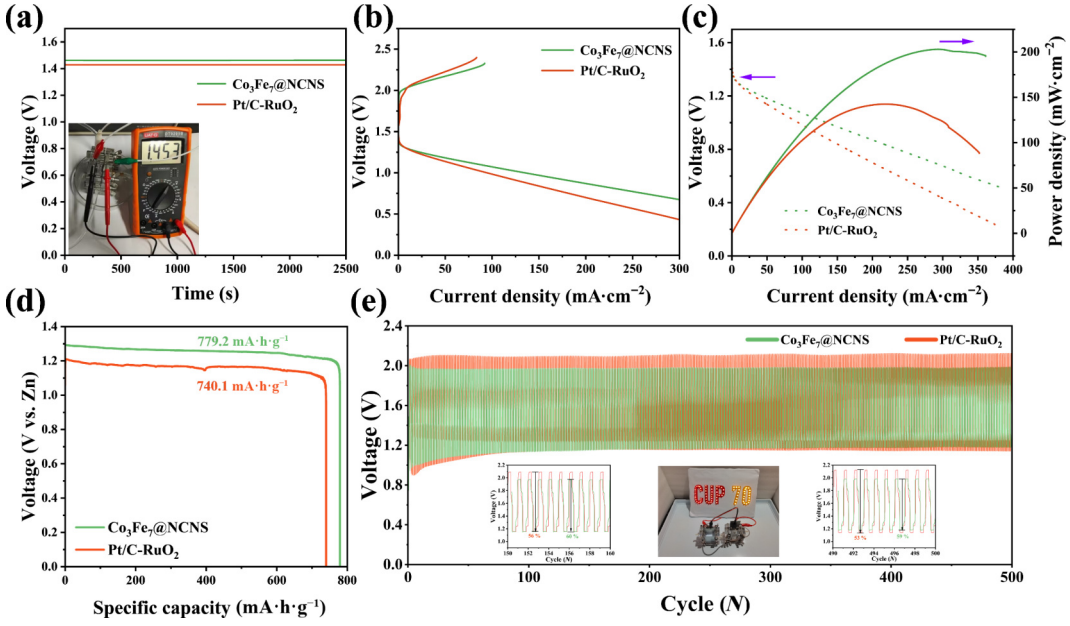

Figure 5 ZAB performance of Co_3Fe_7@NCNS and Pt/C-RuO_2. (a) Open-circuit voltages of Co_3Fe_7@NCNS and Pt/C-RuO_2 based ZABs (the inset shows that the open circuit potential (OCP) of Co_3Fe_7@NCNS is 1.453 V as measured by a multimeter). (b) Charge and discharge polarization curves. (c) Discharge polarization curves and corresponding power density curves of the assembled ZAB. (d) Specific capacity at 5 mA·cm^{-2}. (e) Long-term cycling performance at a current of 5 mA·cm^{-2}, the insets showed the round-trip efficiency of the batteries at 150*N* and 490*N* and a picture of light sign (2.1 V) connected by LED lights operated by two Zn-air batteries.

of 5 mA·cm^{-2} as shown in Fig. 5(e). Co_3Fe_7@NCNS-based battery reflects higher cycle stability compared to Pt/C-RuO_2-based battery in 500 charge–discharge cycle tests (more than 130 h). In particular, the round-trip efficiency (discharge voltage divided by charge voltage) of the Co_3Fe_7@NCNS-equipped battery remains relatively stable after numerous cycles, decreasing from 60% (150*N*–160*N*, *N*: number of cycles of charge and discharge) to 59% (490*N*–500*N*), thereby demonstrating its excellent cycle stability. This efficiency is consistently higher than that of the Pt/C-RuO_2-equipped cell, which ranges from 56% (150*N*–160*N*) to 53% (490*N*–500*N*), as shown in the inset of Fig. 5(e). Additionally, a homemade light sign connected by light-emitting diode (LED) lights can be powered by two series-connected ZABs with Co_3Fe_7@NCNS, as depicted in the inset of Fig. 5(e). The above results strongly demonstrate the feasibility of Co_3Fe_7@NCNS as an excellent ORR/OER bifunctional electrocatalyst assembled into ZAB. Based on the above characterization of the Co_3Fe_7@NCNS catalyst structure and electrocatalytic performance, such as excellent activity and stability of the Co_3Fe_7@NCNS catalyst is mainly attributed to the following reasons. Firstly, the Co_3Fe_7@NCNS catalyst possesses the higher specific surface area and electron transport capacity and the porous nitrogen-doped layered carbon material not only provides sufficient ion transport channels but also improves the dispersion of the active sites and enhances the interaction ability of the active sites with the reactants. Also, the Co_3Fe_7@NCNS catalyst has a special three-dimensional (3D) layered network structure, which can also play a certain mechanical buffering role. This kind of 3D multichannel material can release the tension in time by adjusting the volume of the interlayer, effectively inhibiting electrochemical corrosion of the catalyst and structural damage due to expansion or contraction when used as the cathode of the battery. Secondly, the fully doped nitrogen element further adjusts the electronic structure of its ortho-position carbon element to increase the conductivity, which is beneficial to the OER/ORR reaction. Thirdly, the strong intermetallic forces between the iron and cobalt alloys with excellent crystallinity and the intense interaction with the carbon carrier optimize the adsorption of oxygen intermediates. Finally, CoFe alloy particles coated with ultra-thin carbon layers can greatly improve the stability of the catalyst. A comparison of the ORR performance (Fig. S27 and Table S4 in the ESM) and power density (Fig. S28 and Table S5 in the ESM) of the catalysts in liquid zinc-air batteries in this study with those in the recent literature demonstrates the excellent potential of Co_3Fe_7@NCNS for application in such batteries.

3.4 Theoretical study

DFT calculations were employed to further elucidate the strong interactions between CoFe alloy and nitrogen-doped carbon layers as carrier, which promote the ORR and OER processes of Co_3Fe_7@NCNS. The reaction pathways of OER and ORR on three models were investigated including CoFe alloy particles, Fe_3C and Co NPs encapsulated in nitrogen-doped carbon layers (designated as Co_3Fe_7@NCNS, Fe_3C@NCNS and Co@NCNS, Fig. S29 in the ESM). Figure 6(a) illustrates the evolution paths of three crucial intermediates (O, OOH, OH) on Co_3Fe_7@NCNS during the reverse ORR/OER processes [50, 51]. According to thermodynamic principles, the exothermic pathway among the four fundamental reaction steps ideally belongs to the rate-determining step of ORR, while the endothermic pathway belongs to the rate-determining step of OER [52]. As depicted in Fig. 6(b), the lowest Gibbs free energy change (ΔG_{min}) for all three models occurs in the first step of the ORR reaction, illustrating that the formation of the *OOH intermediate species is the rate-determining step according to DFT calculations. The ΔG_{min} values of Co_3Fe_7@NCNS, Fe_3C@NCNS and Co@NCNS were calculated to be 0.388, 0.260 and 0.044 eV, respectively. It can be concluded from Fig. 6(c) that the rate-determining step of the OER process on all three models is the third step of *O reacting with H_2O to form OOH species, with ΔG_{max} values of 1.953, 2.147 and 2.608 eV, respectively. The result indicates that the formation of *OOH species plays a crucial role in the ORR/OER processes, providing insights for the design of efficient catalysts. Furthermore, these three models were performed by a potential-corrected electrocatalytic step diagram, as shown in Fig. 6(d). All ORR steps on Co_3Fe_7@NCNS, Fe_3C@NCNS and Co@NCNS were downhill at voltage of 0 V, indicating that the ORR reaction is spontaneous [53]. The effective electrode potential

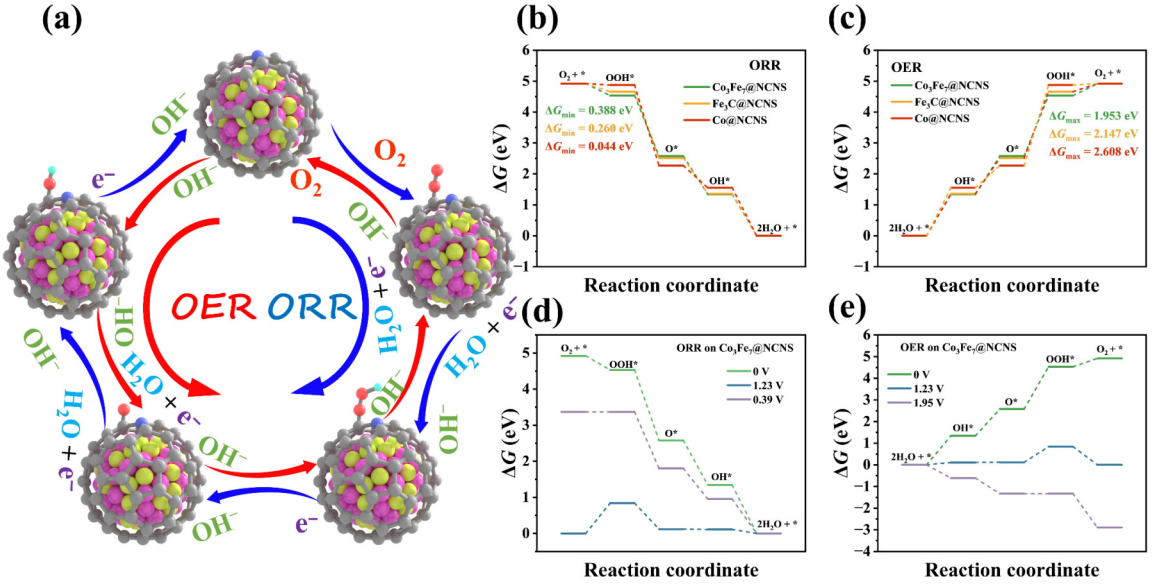

Figure 6 (a) The ORR and OER on the Co_3Fe_7@NCNS (schematic). Blue and red represent the ORR and OER, respectively. The free energy diagram of ORR (b) and OER (c) on three models at electrode potential (U) = 0 V. Changes in the Gibbs free energy (ΔG) during the ORR at U of 0, 1.23 and 1.23 − ηORR (η: overpotential) (d), ΔG during OER (e) at U of 0, 1.23, 1.23 + ηOER.

maintaining each step to be downhill for Co_3Fe_7@NCNS, Fe_3C@NCNS and Co@NCNS were 0.39, 0.26 and 0.04 V, respectively. When the voltage rises to the theoretical potential (1.23 V), all three models exhibit the highest reaction barrier at the first step (transition from O2 to *OOH). The calculated theoretical potential reflects the Co_3Fe_7@NCNS possesses the best ORR activity in these three models. Additionally, as shown in Fig. 6(e), the four OER steps on Co_3Fe_7@NCNS, Fe_3C@NCNS and Co@NCNS were uphill at voltage of 0 V, substantiating that each step of the OER reaction is thermodynamically non-spontaneous. When the potential rises to the equilibrium potential (U = 1.23 V), all models exhibit the highest reaction barrier at the third step (transition from *O to *OOH). To thermodynamically drive each OER step downhill, the energy required with the three models is 1.95, 2.14 and 2.61 V, corresponding to Co_3Fe_7@NCNS, Fe_3C@NCNS and Co@NCNS, respectively (Fig. S30 in the ESM). And it is still the Co_3Fe_7@NCNS reflecting the most excellent OER catalytic ability. Clearly, the DFT computational results corroborate the experimental findings, demonstrating the crucial role of CoFe alloy NPs with strong interactions in enhancing the ORR/OER catalytic capabilities of Co_3Fe_7@NCNS.

4 Conclusion

In conclusion, an excellent oxygen electrode catalyst composed of CoFe alloy particles embedded in nitrogen-doped ultrathin carbon nanosheets are successfully synthesized. Through a meticulously controlled reduction process of CoFe LDH, meticulously obtained via high-temperature hydrothermal treatment, we have achieved the uniform dispersion of CoFe alloy nanoparticles ensconced within a delicately formed carbon matrix. The intricate architecture, featuring interlayer gaps and mesoporous channels within the ultrathin carbon layers, establishes an optimal network for efficient mass transfer. Furthermore, the significant interfacial interaction between alloy nanoparticles and carbon shells enables the optimisation of the electronic structure, thereby enhancing the activity of Co_3Fe_7@NCNS for both the ORR and oxygen OER. Co_3Fe_7@NCNS maintained exceptional ORR catalytic (E_{onset} = 0.962 V, $E_{1/2}$ = 0.869 V), which is compared with the commercial precious metal catalyst Pt/C (E_{onset} = 0.991 V, $E_{1/2}$ = 0.861 V). Furthermore, it exhibits outstanding stability and methanol resistance. Additionally, the Co_3Fe_7@NCNS catalyst showcases remarkable bifunctional activity with a ΔE value of 0.82 V, exceeding monometallic Fe_3C@NCNS-900 and Co@NCNS-900. Most notably, the Co_3Fe_7@NCNS-equipped ZAB delivers a higher open-circuit voltage of 1.46 V and an impressive power density of 202.8 $mW{\cdot}cm^{-2}$ as well as excellent cycling stability compared to Pt/C-RuO_2 counterpart. This study underscores the promise of economically viable and highly efficient transition metal-based materials as air cathodes for ZAB, while also introducing a novel paradigm for electrode material synthesis.

Electronic Supplementary Material: Supplementary material (chemicals details, characterization data, DFT theoretical calculation details, XRD, SEM and TEM images, CV and LSV curves, EIS and activity comparison chart) is available in the online version of this article at https://doi.org/10.26599/NR.2025.94907139.

Data availability

All data needed to support the conclusions in the paper are presented in the manuscript and the Electronic Supplementary Material.

Acknowledgements

The authors gratefully acknowledge the financial support from National Key Research and Development Program of China (No. 2021YFA1501304) and the National Natural Science Foundation of China (Nos. 22035009 and 22122113). We thank Quantum Design (Beijing) Co., Ltd. for their assistance with X-ray absorption spectroscopy (XAS) measurements, as well as support throughout the data processing and analysis phases. We also sincerely thank Professor Guanghui Zhang of Dalian University of Technology for his guidance on XAS analysis.

Declaration of competing interest

All the contributing authors report no conflict of interests in this work.

Author contribution statement

P. L. L.: Writing – original draft, formal analysis, data curation. Y. Q. S.: Supervision, formal analysis, writing – review & editing, project administration. J. Q. L.: Software, conceptualization. Z. H. D.: Conceptualization, data curation. P. Z.: Formal analysis. S. M. Z.: Data curation. Y. C. W.: Methodology. W. Y. S.: Methodology. Y. W.: Software. Z. X. L.: Supervision, formal analysis. Z. Z.: Methodology. J. L.: Supervision, methodology, funding acquisition.

Use of AI statement

None.

References

[1] Bi, X. X.; Jiang, Y.; Chen, R. T.; Du, Y. C.; Zheng, Y.; Yang, R.; Wang, R. Y.; Wang, J. T.; Wang, X.; Chen, Z. W. Rechargeable zinc-air versus lithium-air battery: From fundamental promises toward technological potentials. *Adv. Energy Mater.* **2024**, *14*, 2302388.

[2] Nazir, G.; Rehman, A.; Lee, J. H.; Kim, C. H.; Gautam, J.; Heo, K.; Hussain, S.; Ikram, M.; AlObaid, A. A.; Lee, S. Y. et al. A review of rechargeable zinc-air batteries: Recent progress and future perspectives. *Nano-Micro Lett.* **2024**, *16*, 138.

[3] Liu, H. B.; Xie, R. X.; Niu, Z. Q.; Jia, Q. H.; Yang, L.; Wang, S. T.; Cao, D. P. Two-in-one strategy to construct bifunctional oxygen electrocatalysts for rechargeable Zn-air battery. *Chin. J. Catal.* **2022**, *43*, 2906–2912.

[4] Meng, H. L.; Lin, S. Y.; Cao, Y.; Wang, A. J.; Zhang, L.; Feng, J. J. CoFe alloy embedded in N-doped carbon nanotubes derived from triamterene as a highly efficient and durable electrocatalyst beyond commercial Pt/C for oxygen reduction. *J. Colloid Interface Sci.* **2021**, *604*, 856–865.

[5] Huang, H. J.; Yu, D. S.; Hu, F.; Huang, S. C.; Song, J. N.; Chen, H. Y.; Li, L. L.; Peng, S. J. Clusters induced electron redistribution to tune oxygen reduction activity of transition metal single-atom for metal-air batteries. *Angew. Chem., Int. Ed.* **2022**, *61*, e202116068.

[6] Cherevko, S.; Geiger, S.; Kasian, O.; Kulyk, N.; Grote, J. P.; Savan, A.; Shrestha, B. R.; Merzlikin, S.; Breitbach, B.; Ludwig, A. et al. Oxygen and hydrogen evolution reactions on Ru, RuO_2, Ir, and IrO_2 thin film electrodes in acidic and alkaline electrolytes: A comparative study on activity and stability. *Catal. Today* **2016**, *262*, 170–180.

[7] An, Z.; Li, H. Q.; Zhang, X. M.; Xu, X. L.; Xia, Z. X.; Yu, S. S.; Chu, W. L.; Wang, S. L.; Sun, G. Q. Structural evolution of a PtRh

nanodendrite electrocatalyst and its ultrahigh durability toward oxygen reduction reaction. *ACS Catal.* **2022**, *12*, 3302–3308.

[8] Nie, Y.; Sun, Y. J.; Song, B. Y.; Meyer, Q.; Liu, S. Y.; Guo, H. Y.; Tao, L.; Lin, F. X.; Luo, M. C.; Zhang, Q. H. et al. Low-electronegativity Mn-contraction of PtMn nanodendrites boosts oxygen reduction durability. *Angew. Chem., Int. Ed.* **2024**, *63*, e202317987.

[9] Chen, Z. G.; Zhao, J.; Jin, C.; Liu, J. J. Butterfly effect of electron donor from monoatomic cobalt in few-atom platinum clusters: Boosting electrocatalysis. *ACS Appl. Mater. Interfaces* **2022**, *14*, 37727–37737.

[10] Cao, D. L.; Mu, Y. W.; Liu, L. J.; Mou, Z. X.; Chen, S.; Yan, W. J.; Zhou, H. Q.; Chan, T. S.; Chang, L. Y.; Song, L. et al. Axially modified square-pyramidal CoN_4–F_1 sites enabling high-performance Zn-air batteries. *ACS Nano* **2024**, *18*, 11474–11486.

[11] Chen, P. Z.; Tong, Y.; Wu, C. Z.; Xie, Y. Surface/interfacial engineering of inorganic low-dimensional electrode materials for electrocatalysis. *Acc. Chem. Res.* **2018**, *51*, 2857–2866.

[12] Zhang, S.; Wang, W.; Hu, F.; Mi, Y.; Wang, S.; Liu, Y.; Ai, X.; Fang, J.; Li, H.; Zhai, T. 2D CoOOH sheet-encapsulated Ni_2P into tubular arrays realizing 1000 $mA{\cdot}cm^{-2}$-level-current-density hydrogen evolution over 100 h in neutral water. *Nano-Micro Lett.* **2020**, *12*, 140.

[13] Zhao, C. X.; Li, B. Q.; Liu, J. N.; Zhang, Q. Intrinsic electrocatalytic activity regulation of M–N–C single-atom catalysts for the oxygen reduction reaction. *Angew. Chem., Int. Ed.* **2021**, *60*, 4448–4463.

[14] Sun, Y. Q.; Ouyang, Y. M.; Luo, J. Q.; Cao, H. H.; Li, X.; Ma, J. W.; Liu, J.; Wang, Y. H.; Lu, L. Biomass-derived nitrogen self-doped porous activation carbon as an effective bifunctional electrocatalysts. *Chin. Chem. Lett.* **2021**, *32*, 92–98.

[15] Zhu, S.; Ding, L. T.; Zhang, X. H.; Wang, K.; Wang, X.; Yang, F.; Han, G. Y. Biaxially-strained phthalocyanine at polyoxometalate @carbon nanotube heterostructure boosts oxygen reduction catalysis. *Angew. Chem.* **2023**, *135*, e202309545.

[16] Li, L. B.; Tang, X. N.; Huang, S. H.; Lu, C. B.; Lützenkirchen-Hecht, D.; Yuan, K.; Zhuang, X. D.; Chen, Y. W. Longitudinally grafting of graphene with iron phthalocyanine-based porous organic polymer to boost oxygen electroreduction. *Angew. Chem., Int. Ed.* **2023**, *62*, e202301642.

[17] Li, J. K.; Sougrati, M. T.; Zitolo, A.; Ablett, J. M.; Oğuz, I. C.; Mineva, T.; Matanovic, I.; Atanassov, P.; Huang, Y.; Zenyuk, I. et al. Identification of durable and non-durable FeN_x sites in Fe–N–C materials for proton exchange membrane fuel cells. *Nat. Catal.* **2021**, *4*, 10–19.

[18] Li, H.; Shu, X. X.; Tong, P. R.; Zhang, J. H.; An, P. F.; Lv, Z. X.; Tian, H.; Zhang, J. T.; Xia, H. B. Fe–Ni alloy nanoclusters anchored on carbon aerogels as high-efficiency oxygen electrocatalysts in rechargeable Zn-air batteries. *Small* **2021**, *17*, 2102002.

[19] Wang, J. B.; Zhang, Y. N.; Guo, X.; Liao, S. Q.; Lv, P. F.; Wei, Q. F. FeCo/N-co-doped 3D carbon nanofibers as efficient bifunctional oxygen electrocatalyst for Zn-air batteries. *Nanoscale* **2023**, *15*, 625–630.

[20] Hu, J.; Zhang, C. X.; Sun, M. Z.; Qi, Q. L.; Luo, S. X.; Song, H. C.; Xiao, J. Y.; Huang, B. L.; Leung, M. K. H.; Zhang, Y. J. Ultrastable bimetallic Fe_2Mo for efficient oxygen reduction reaction in pH-universal applications. *Nano Res.* **2022**, *15*, 4950–4957.

[21] Pei, Z. H.; Lu, X. F.; Zhang, H. B.; Li, Y. X.; Luan, D. Y.; Lou, X. W. Highly efficient electrocatalytic oxygen evolution over atomically dispersed synergistic Ni/Co dual sites. *Angew. Chem., Int. Ed.* **2022**, *134*, e202207537.

[22] Tian, Y. H.; Wu, Z. Z.; Li, M.; Sun, Q.; Chen, H.; Yuan, D. J.; Deng, D.; Johannessen, B.; Wang, Y.; Zhong, Y. L. et al. Atomic modulation and structure design of Fe-N_4 modified hollow carbon fibers with encapsulated Ni nanoparticles for rechargeable Zn-air batteries. *Adv. Funct. Mater.* **2022**, *32*, 2209273.

[23] Su, C. Y.; Cheng, H.; Li, W.; Liu, Z. Q.; Li, N.; Hou, Z. F.; Bai, F. Q.; Zhang, H. X.; Ma, T. Y. Atomic modulation of FeCo–nitrogen–carbon bifunctional oxygen electrodes for rechargeable and flexible all-solid-state zinc-air battery. *Adv. Energy Mater.* **2017**, *7*, 1602420.

[24] Deng, C.; Tan, J. J.; Toe, C. Y.; Li, X.; Li, G. D.; Jiang, X. X.; Wei, S. M.; Yang, H. P.; Hu, Q.; He, C. X. Achieving efficient oxygen reduction on ultra-low metal-loaded electrocatalysts by constructing well-dispersed bimetallic sites and interconnected porous channels. *J. Mater. Chem. A* **2022**, *10*, 17217–17224.

[25] Chang, H.; Zhao, L. L.; Zhao, S.; Liu, Z. L.; Wang, P. F.; Xie, Y.; Yi, T. F. Tuning interface mechanism of FeCo alloy embedded N,S-codoped carbon substrate for rechargeable Zn-air battery. *J. Energy Chem.* **2024**, *93*, 400–410.

[26] Wen, J. K.; Li, X. F.; Liu, Y. J.; Yang, M.; Liu, B.; Chen, H. B.; Li, H. M. Facile crafting of ultralong N-doped carbon nanotube encapsulated with FeCo nanoparticles as bifunctional electrocatalyst for rechargeable zinc-air batteries. *Microporous Mesoporous Mater.* **2022**, *336*, 111850.

[27] Li, Z. Y.; Yang, H. Q.; Sun, H.; Liang, S.; Lu, G. L.; Liu, Z. N.; Kou, S. Q. Highly nitrogen-doped carbon nanotube nanoarrays as self-supported bifunctional electrocatalysts for rechargeable and flexible zinc-air batteries. *ACS Sustain. Chem. Eng.* **2021**, *9*, 4498–4508.

[28] Huang, W. F.; Hai, B.; Su, G. E.; Mao, H. L.; Li, J. F. P-doped Fe–N–C catalysts as advanced bifunctional electrocatalyst for ORR, OER and Zn-air batteries. *Mater. Lett.* **2024**, *360*, 135976.

[29] Xia, J. Y.; Li, C.; Gong, Y. Y.; Niu, L. Y.; Chen, M. G.; Xu, S. Q. Designing of highly-efficient oxygen evolution reaction electrocatalyst FeCo-hydroxyl phosphates: Theory and experiment. *Chem. Eng. J.* **2022**, *446*, 137151.

[30] Cai, S. C.; Meng, Z. H.; Li, G. J.; An, Y.; Cheng, Y. P.; Kan, E. J.; Ouyang, B.; Zhang, H. N.; Tang, H. L. Nitrogen doped porous carbon-based bifunctional oxygen electrocatalyst with controllable phosphorus content for zinc-air battery. *Nano Res.* **2023**, *16*, 5887–5893.

[31] Hao, X. Q.; Jiang, Z. Q.; Zhang, B. A.; Tian, X. N.; Song, C. S.; Wang, L. K.; Maiyalagan, T.; Hao, X. G.; Jiang, Z. J. N-doped carbon nanotubes derived from graphene oxide with embedment of FeCo nanoparticles as bifunctional air electrode for rechargeable liquid and flexible all-solid-state zinc-air batteries. *Adv. Sci.* **2021**, *8*, 2004572.

[32] Guo, D. H.; Shibuya, R.; Akiba, C.; Saji, S.; Kondo, T.; Nakamura, J. Active sites of nitrogen-doped carbon materials for oxygen reduction reaction clarified using model catalysts. *Science* **2016**, *351*, 361–365.

[33] Liu, X. P.; Liu, Y. P.; Zhang, C. C.; Chen, Y.; Luo, G. Y.; Wang, Z. T.; Wang, D. L.; Gao, S. Y. N, S co-doped hollow carbon nanocages confined Fe, Co bimetallic sites for bifunctional oxygen electrocatalysis. *Chem. Eng. J.* **2023**, *473*, 145135.

[34] Lin, L. G.; Xue, P.; Cui, X. M.; Liu, J. H.; Liu, J. J.; Tang, M.; Wang, Z. B. Controllable construction of FeCo nanoparticles embedded 3D porous N-doped carbon nanonetworks as high efficiency bifunctional electrocatalysts for Zn-air batteries. *J. Alloys Compd.* **2022**, *909*, 164625.

[35] Sun, L.; Dang, Y.; Wu, A. P.; Tian, C. G.; Wang, D. X.; Yan, H. J.; Gao, Y. C.; Fu, H. G. Synchronous regulation of morphology and electronic structure of FeNi–P nanosheet arrays by Zn implantation for robust overall water splitting. *Nano Res.* **2023**, *16*, 5733–5742.

[36] Fuertes, A. B.; Ferrero, G. A.; Sevilla, M. One-pot synthesis of microporous carbons highly enriched in nitrogen and their electrochemical performance. *J. Mater. Chem. A* **2014**, *2*, 14439–14448.

[37] Luo, J. Q.; Sun, Y. Q.; Liu, P. L.; Zhong, S. M.; Li, Y. G.; Zhang, R. L.; Zhang, P.; Chi, Y. L.; Xu, H.; Wei, Y. C. et al. Nitrogen-containing-defect-site-assisted H_2O adsorption and dissociation on crystalline Ru nanoclusters by quasi-hydrogen bonds boosts alkaline hydrogen evolution reaction. *ACS Sustain. Chem. Eng.* **2024**, *12*, 5319–5331.

[38] Deng, D. H.; Yu, L.; Chen, X. Q.; Wang, G. X.; Jin, L.; Pan, X. L.; Deng, J.; Sun, G. Q.; Bao, X. H. Iron encapsulated within pod-like

carbon nanotubes for oxygen reduction reaction. *Angew. Chem., Int. Ed.* **2013**, *52*, 371–375.

[39] Li, Z. T.; Wei, L. Q.; Jiang, W. J.; Hu, Z. P.; Luo, H.; Zhao, W. N.; Xu, T.; Wu, W. T.; Wu, M. B.; Hu, J. S. Chemical state of surrounding iron species affects the activity of Fe–N_x for electrocatalytic oxygen reduction. *Appl. Catal. B: Environ.* **2019**, *251*, 240–246.

[40] Li, X.; Ma, J. W.; Luo, J. Q.; Cheng, S. T.; Gong, H. Z.; Liu, J.; Xu, C. M.; Zhao, Z.; Sun, Y. Q.; Song, W. Y. et al. Porous N, P co-doped carbon-coated ultrafine Co_2P nanoparticles derived from DNA: An electrocatalyst for highly efficient hydrogen evolution reaction. *Electrochim. Acta* **2021**, *393*, 139051.

[41] Luo, J. Q.; Liu, C. Y.; Zhang, R. L.; Sun, Y. Q.; Xu, H.; Hu, Q. Y.; Zhang, M. X.; Li, J.; Li, Z. X.; Song, W. Y. et al. Efficient contact between H_2O and N-coordinate Ru nanoparticles in three-dimensionally ordered macro/mesoporous carbon boosting alkaline HER†. *Chin. J. Chem.* **2024**, *42*, 164–170.

[42] Wang, Y. X.; Zhang, Y.; Xing, P. Y.; Li, X. Q.; Du, Q. Y.; Fan, X. Q.; Cai, Z. B.; Yin, R.; Yao, Y. G.; Gan, W. T. Self-encapsulation of high-entropy alloy nanoparticles inside carbonized wood for highly durable electrocatalysis. *Adv. Mater.* **2024**, *36*, 2402391.

[43] Zheng, Y. J.; Wang, P.; Huang, W. H.; Chen, C. L.; Jia, Y. Y.; Dai, S.; Li, T.; Zhao, Y.; Qiu, Y. C.; Waterhouse, G. I. N. et al. Toward more efficient carbon-based electrocatalysts for hydrogen peroxide synthesis: Roles of cobalt and carbon defects in two-electron ORR catalysis. *Nano Lett.* **2023**, *23*, 1100–1108.

[44] Wang, M.; Liu, B. L.; Zhang, H. Y.; Lu, Z. J.; Xie, J.; Cao, Y. L. High quality bifunctional cathode for rechargeable zinc-air batteries using N-doped carbon nanotubes constrained CoFe alloy. *J. Colloid Interface Sci.* **2024**, *661*, 681–689.

[45] Xu, X. Q.; Xie, J. H.; Liu, B.; Wang, R. Y.; Liu, M. Y.; Zhang, J.; Liu, J.; Cai, Z.; Zou, J. L. PBA-derived FeCo alloy with core–shell structure embedded in 2D N-doped ultrathin carbon sheets as a bifunctional catalyst for rechargeable Zn-air batteries. *Appl. Catal. B: Environ.* **2022**, *316*, 121687.

[46] Chen, J. X.; Zhu, J.; Li, S. J.; Li, Z. L.; Wu, C. Z.; Wang, D.; Luo, Z. H.; Li, Y. B.; Luo, K. *In situ* construction of FeCo alloy nanoparticles embedded in nitrogen-doped bamboo-like carbon nanotubes as a bifunctional electrocatalyst for Zn-air batteries. *Dalt. Trans.* **2022**, *51*, 14498–14507.

[47] Park, J. H.; Ro, J. C.; Suh, S. J. FeCo nanoparticles with different compositions as electrocatalysts for oxygen evolution reaction in alkaline solution. *Appl. Surf. Sci.* **2022**, *589*, 153041.

[48] Zhao, S. N.; Li, J. K.; Wang, R.; Cai, J. M.; Zang, S. Q. Electronically and geometrically modified single-atom Fe sites by adjacent Fe nanoparticles for enhanced oxygen reduction. *Adv. Mater.* **2022**, *34*, 2107291.

[49] Gomaa, H.; An, C. H.; Jiao, P. G.; Wu, W. L.; Alzahrani, H. A. H.; Shenashen, M. A.; Deng, Q. B.; Hu, N. Controllable synthesis of a hybrid mesoporous sheets-like $Fe_{0.5}NiS_2$@P,N-doped carbon electrocatalyst for alkaline oxygen evolution reaction. *J. Colloid Interface Sci.* **2024**, *667*, 166–174.

[50] Wang, S. J.; Wang, H. Y.; Huang, C. Q.; Ye, P. C.; Luo, X. T.; Ning, J. Q.; Zhong, Y. J.; Hu, Y. Trifunctional electrocatalyst of N-doped graphitic carbon nanosheets encapsulated with CoFe alloy nanocrystals: The key roles of bimetal components and high-content graphitic-N. *Appl. Catal. B: Environ.* **2021**, *298*, 120512.

[51] Xie, D. Y.; Yu, D. S.; Hao, Y. N.; Han, S. L.; Li, G. H.; Wu, X. L.; Hu, F.; Li, L. L.; Chen, H. Y.; Liao, Y. F. et al. Dual-active sites engineering of N-doped hollow carbon nanocubes confining bimetal alloys as bifunctional oxygen electrocatalysts for flexible metal-air batteries. *Small* **2021**, *17*, e2007239.

[52] Sun, Y. Q.; Luo, J. Q.; Zhang, M. X.; Li, J.; Yu, J. K.; Lu, S. Y.; Song, W. Y.; Wei, Y. C.; Li, Z. X.; Liu, J. Electron delocalization of Au nanoclusters triggered by Fe single atoms boosts alkaline overall water splitting. *ACS Appl. Mater. Interfaces* **2023**, *15*, 10696–10708.

[53] Zhang, D.; Wang, Z. Y.; Liu, F. Z.; Yi, P. Y.; Peng, L. F.; Chen, Y.; Wei, L.; Li, H. Unraveling the pH-dependent oxygen reduction performance on single-atom catalysts: From single- to dual-Sabatier optima. *J. Am. Chem. Soc.* **2024**, *146*, 3210–3219.